Supporting Information:

How Actuated Particles Effectively Capture Biomolecular Targets

Alexander van Reenen[1,2], Arthur M. de Jong[1,2], Menno W. J. Prins[1,2,3*]

[1] Department of Applied Physics, Eindhoven University of Technology, 5600 MB Eindhoven, The Netherlands

[2] Institute for Complex Molecular Systems, Eindhoven University of Technology, 5600 MB Eindhoven, The Netherlands

[3] Department of Biomedical Engineering, Eindhoven University of Technology, 5600 MB Eindhoven, The Netherlands

*corresponding author:
e-mail: m.w.j.prins@tue.nl

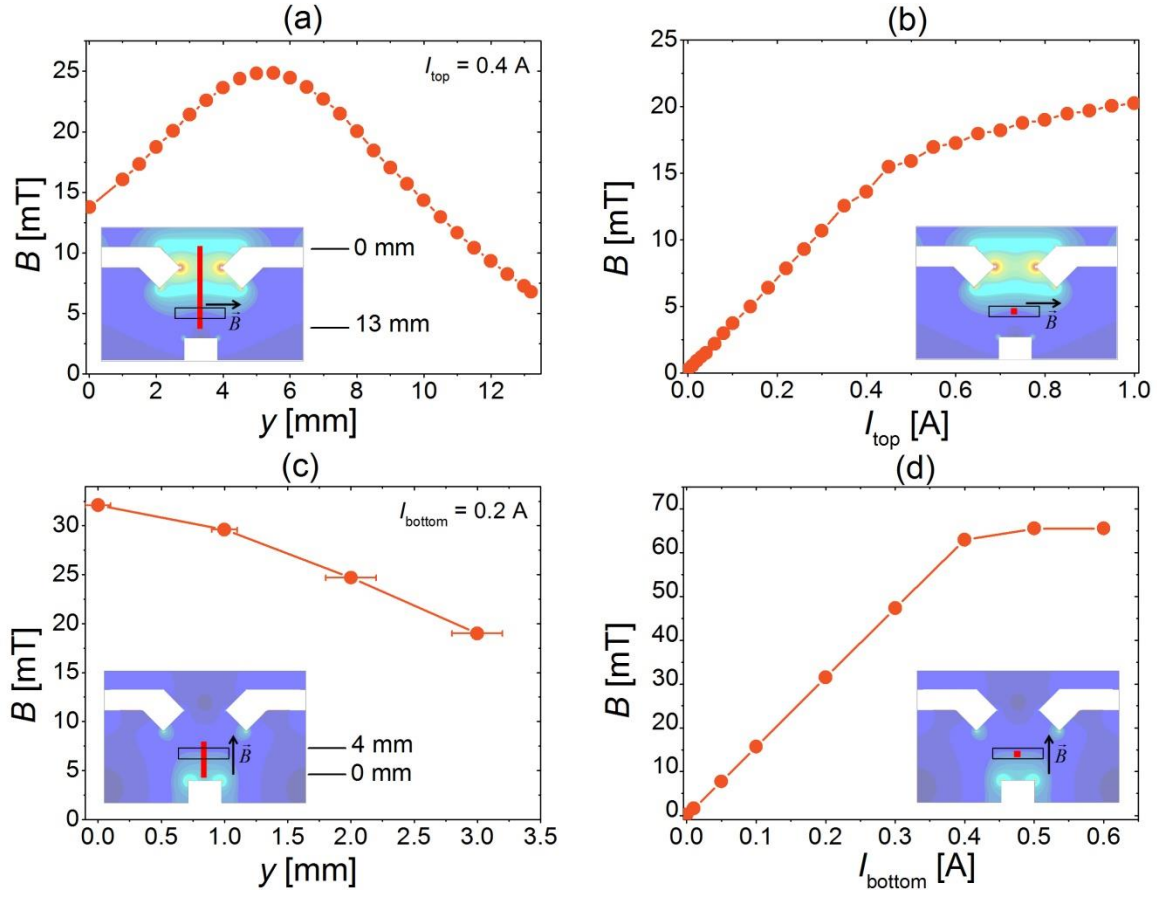# S1 Field calibration of the 5-pole electromagnet

Figure S1 Field calibration data of the 5-pole electromagnet measured using a Gauss meter (F.W. Bell). In each calibration figure the inset shows a cross-section of the electromagnets (showing two top magnets and the bottom magnet). The cross-sectional views show the position (red rectangles) and the component (black arrows) of the measured field. The location of the incubation chamber is indicated by the black open rectangle. In the background of the cross-sectional views, the (relative) field strength is plotted (following a heat color map) as obtained from simulations using Comsol Multiphysics. The following field calibrations are shown in the different panels: (a) In-plane field dependence of the distance from the top magnets for the case two opposite top magnets are powered in series at $I_{top} = 0.4$ A. (b) The in-plane field dependence to the current I_{top} at the position of the incubation chamber, for the case two opposite top magnets are powered in series. (c) Dependence of the out-of-plane field to the distance from the bottom magnet for the case that only the bottom magnet is powered at $I_{bottom} = 0.2$ A. (d) Dependence of the out-of-plane field to the current I_{bottom} at the position of the incubation chamber, for the case that only the bottom magnet is powered.

S2 Rotaphoresis to redistribute particles

To overcome the effects of particle drift and particle aggregation during actuation, we applied the method of magnetic rotaphoresis as is described in detail in ref[1]. Here, we will briefly summarize the applied fields and the effects.
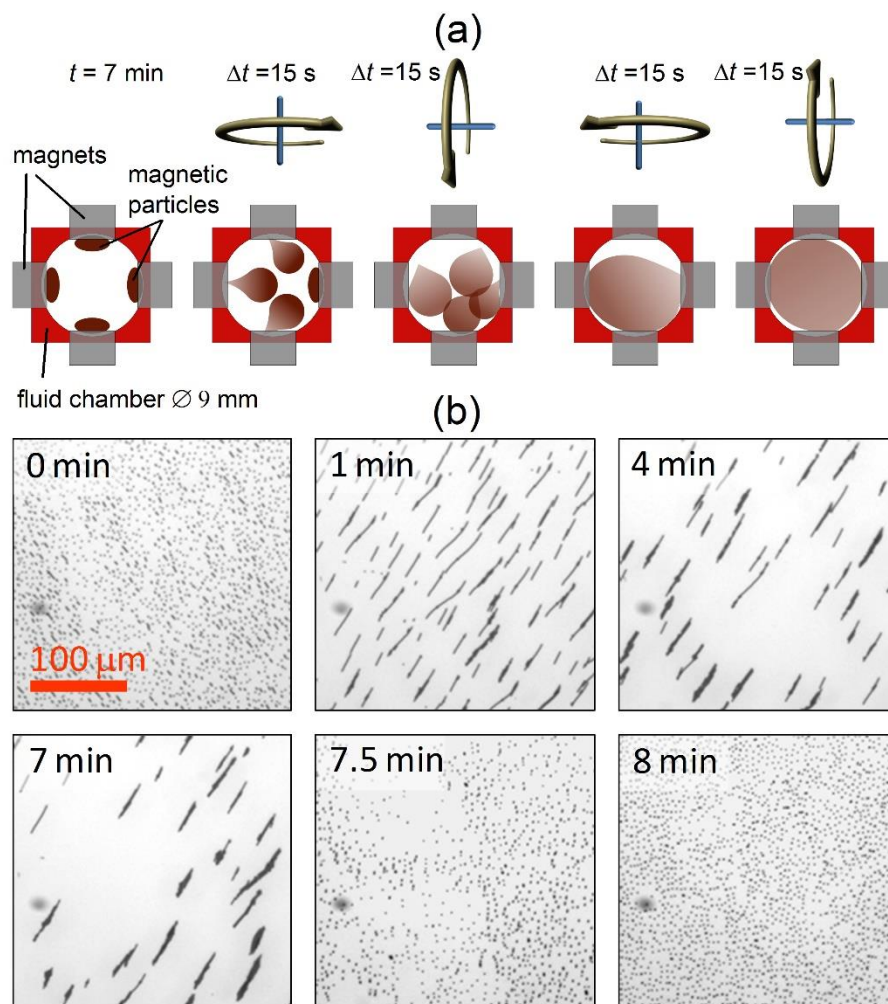

Figure S2 Overview of the applied rotaphoresis to redistribute particles over the bottom surface of the incubation chamber after magnetic actuation for target capture. (a) Schematic representation of the applied actuation protocol and the effect on the particle distribution (from left to right), in case initially all particles (brown) are collected at the magnets (gray) on all four sides. As indicated by the arrows, rotaphoresis was applied towards each magnet for 15 seconds to move all particles away from the side of the incubation chamber. (b) Microscope images of magnetic chain actuation followed after 7 minutes by particle redistribution by rotaphoresis. The used microscope objective magnification was 10 times and images of the bottom-center of the incubation chamber were taken by a Redlake MotionPro X3 high speed camera. At t = 0 min, magnetic field of 10 mT was applied, rotating in-plane with respect to the surface at a frequency of 0.1 Hz. At t = 7 min, rotaphoresis was applied for 1 minute: 15 seconds in each direction in-plane.

Basically, the rotaphoretic protocol that was applied consisted of the following elements: (i) a field gradient of ~ 4 T/m oriented towards the surface, in order to bring and keep particles close to the surface (x,y-plane); (ii) a magnetic field rotating out-of-plane (e.g. x,z-plane) with respect to the surface at 20 Hz, with an out-of-plane (z) component of 15 mT and an in-plane (x) component of 6 mT; (iii) an alternating magnetic field orthogonal to the applied rotating field, e.g. in the y-direction in case the field rotates in the x,z-plane. The effect of such a protocol on magnetic particles is the following. Chains of particles traverse or "walk" over the surface in the direction depending on the rotation of the magnetic field. The velocity of the particle chains depends on their size: larger chains move faster than smaller chains, and separate particles are nearly immobile. Furthermore, due to the hydrodynamic drag and the normal forces from the surface, particle chains break up in smaller chains, and eventually most particles split up in separate particles. Finally, as the out-of-plane (z) component of the magnetic field with respect to the surface is larger than the in-plane components, separate particles will repel each other more strongly than that they will attract each other when the field is oriented in-plane. This effect prevents redistributed particles to reform into chains while the rotaphoresis protocol is applied.

Lastly, in order to redisperse particles from all magnet poles back into the incubation chamber and over the whole bottom surface, the rotaphoretic protocol was applied in all directions (in-plane; see Figure S2a). More specifically, rotaphoresis was applied to first move particles consecutively in the $+x$-direction, the $-y$-direction, the $-x$-direction and the $+y$-direction. Rotaphoresis was applied for 15 seconds in each direction, resulting in a total time of 1 minute to redistribute particles over the surface.

In Figure S2b, snapshots are shown of a magnetic actuation protocol that first consists of magnetic chain actuation for target capture (i.e. for the first 7 minutes), followed by one minute of rotaphoresis. As shown, magnetic chain actuation first causes particles to form chain-like aggregates that drift away from the center of the incubation chamber. Application of the above-described rotaphoresis protocol causes a complete redistribution of the particles over the surface.

S3 Image processing to determine particle fluorescence

Images such as shown in Figure S3a were individually processed using ImageJ and Matlab software to determine the average fluorescence intensity of the particles with respect to the background which surrounds the particles in the images. First, the area occupied by the magnetic particles was determined by making a binary image using ImageJ (see Figure S3b,c). Subsequently Matlab software was used to determine the average intensity of the pixels corresponding to the particles or the background. In Figure S3d the average intensity of the particles with respect to the background is shown for different thresholds to obtain the binary image. Based on this, a relative error of 10% is estimated for a single measurement of the fluorescence coming off the particles. As the intensity is averaged over the number of pixels, a single measurement is independent of the number of particles within a single field of view.
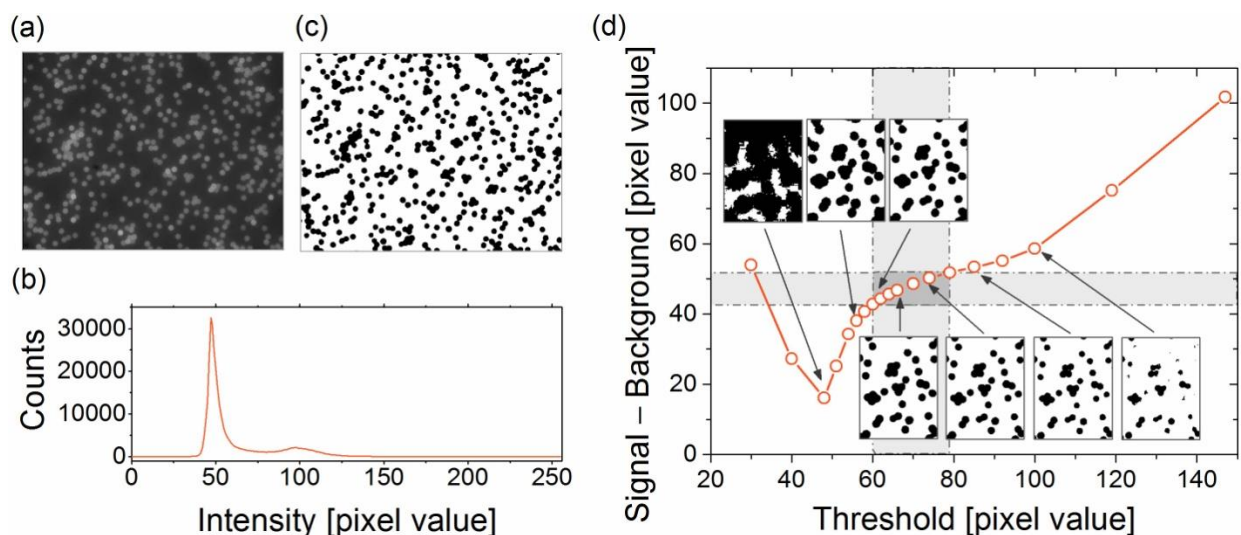

Figure S3 Image processing to determine the fluorescence of the magnetic particles with respect to the background. (a) Original fluorescence image (b) Histogram of pixel intensities for the original image. By setting a threshold in between the two peaks, i.e., at a pixel value of 70, (c) a binary image is obtained. The binary image is used as a mask to determine the fluorescence signal from the particles and the surrounding background. In (d) the average pixel intensity of the particles with respect to the background is shown for different values of the threshold for the binary image. Corresponding binary images are shown for several data-points. The gray bars indicate the region in which the threshold results in binary images containing particles with sizes that are approximately equal compared to the fluorescence images.

S4 Control experiments to verify binding specificity

We compared target capture with our experimental model system to several control experiments, to investigate whether capture was specific. In each measurement equal concentrations of reagents were incubated in a micro-centrifuge tube on a vortex mixer (mixing at 1400 rpm for 30 minutes). After incubation, the magnetic particles were washed magnetically, re-suspended in assay buffer and pipetted in an incubation chamber. After sedimentation, fluorescence images of the particles were recorded and fluorescence signals were determined.

First, we tested different surface functionalizations of the particles: see the white bars in Figure S4. A clear increase in signal was found for protein G-coated particles compared to the other surface functionalizations. The relatively high signal for the controls can be mainly attributed to the autofluorescence of the magnetic particles; compare the black bar in Figure S4. Lastly, we also included a measurement of the protein G-coated particles for the case of 30 minutes of magnetic actuation: the 6th (orange) bar. Interestingly, magnetic actuation shows a larger increase in target capture compared to vortex mixing. This is already a first indication of the effectiveness of magnetic actuation in target capture.
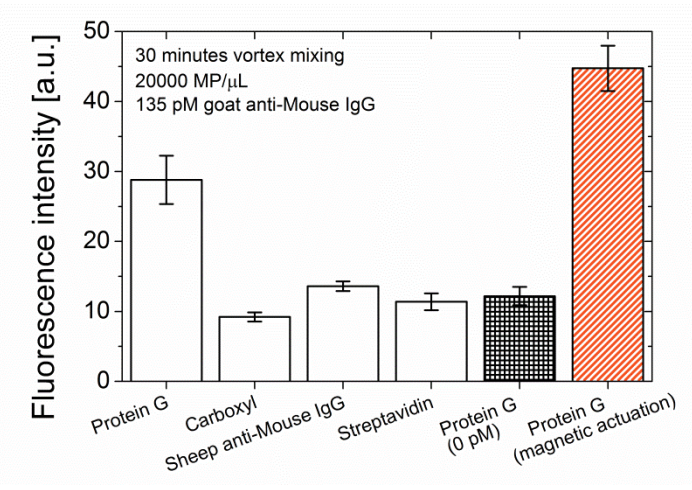

Figure S4 Control experiments for the specificity of the experimental model system: goat anti-mouse IgG and protein G-coated magnetic particles. The average particle fluorescence was measured after 30 minutes of incubation of the reagents on a vortex mixer, except for the orange bar. Different surface functionalizations were tested: protein G; carboxyl (hydrophilic); sheep anti-mouse IgG and streptavidin. To determine the contribution to the fluorescence intensity due to the auto-fluorescence of the magnetic particles, a measurement was performed with a zero target concentration (i.e. the black bar). The error bars correspond to the standard deviation in the determined fluorescence intensity.

S5 Determination of rate constants for association and dissociation

From the experimental data, rate constants were determined by analyzing the time-dependence of the fluorescence intensity of the particles. The kinetic analysis is based on the overall association reaction between a magnetic particle (MP) and an antibody (Ab), described as

$$\text{MP} + \text{Ab} \quad \underset{k_d}{\overset{k_a}{\rightleftharpoons}} \quad \text{MPAb} , \tag{S.1}$$

in which k_a and k_d respectively are the association rate constant and the dissociation rate constant. Based on this equation, the rate at which antibodies are captured and bound to magnetic particles is:

$$\frac{\mathrm{d}\left[\text{boundAb}\right]}{\mathrm{d}t} = k_a\left[\text{Ab}\right]\left[\text{MP}\right]\theta - k_d\left[\text{boundAb}\right]. \tag{S.2}$$

Here, the brackets indicate concentrations of the different species, which depend on time. In Eq. S.2, [boundAb] is used instead of [MPAb] to better express that multiple antibodies can bind to the same magnetic particle. To account for saturation of the particle surface, the term θ is included in Eq. S.2, which represents the ratio between the number of free and accessible binding sites compared to the total number of binding sites (i.e. free, occupied or inaccessible). Initially, θ is equal to 1, but its value drops to zero as the particle surface becomes saturated and covered by bound antibodies. In experiments we used a [MP]:[Ab] ratio of 1:5000, and compared to the determined binding capacity of $(1.8 \pm 0.2) \times 10^5$ antibodies per magnetic particle, we estimate that only 3% or less of the available binding sites will react. Based on these considerations, we assume that $\theta = 1$ in our experiments. The corresponding solution of Eq. S.2 then is:

$$[\text{boundAb}] = \frac{k_a[\text{MP}][\text{Ab}]}{k_a[\text{MP}] + k_d}\left(1 - \exp\left(-\left(k_a[\text{MP}] + k_d\right)t\right)\right). \tag{S.3}$$

Assuming that [boundAb] scales linearly with the particle fluorescence, Eq. S.3 can be applied to experimental data to extract both the association and the dissociation rate constants. However, this is only possible when the exponential behavior is observed, as the initial rate of the kinetic regime (i.e. the limit of small t) does not depend on the dissociation rate constant, but only on the association rate constant.

S6 Comparison of particle-based capture with planar surface assays

We compare the kinetic analysis of particle-based target capture to a technique that is typically used to quantify rate constants of biomolecular reactions, namely surface plasmon resonance (SPR).[2] In SPR, targets are captured from a fluid flow by biomolecules which are immobilized on a planar sensor surface. This process has similarities to target capture by actuated magnetic particles. Conversely, no magnetic actuation corresponds to SPR without a fluid flow, which generally results in the formation of target depletion zones near the sensor surface. Concerning the assay kinetics in SPR (i.e., with a fluid flow), the concentration of targets in solution is dominant over the number of binding sites on the solid phase, in contrast to our experiments, where targets are only few compared to the number that can be bound in total by the magnetic particles. As a result, in SPR analysis an equation is used other than Eq. 6, because the exponential behavior in SPR depends on the target concentration instead of the concentration of magnetic particles or binding sites; i.e., [MP] should be replaced by [Ab].

SPR data allow one to determine rate constants without quantifying the number of binding sites on the bio-functionalized surface. It should be noted however, that the determined rate constants do not completely represent the rate constants of the bimolecular reaction free in solution. For example, the fact that and the way in which biomolecules are attached to the surface affect the rate constants, but also the application of a fluid flow has an effect on the encounter rate.

In the current study, we are not primarily interested in the bimolecular association rate between the targets and the proteins immobilized on the particle surface. Instead, we are primarily interested in the association rate between targets and a particle. This association process is made selective by using proteins with a particular specificity to the targets. Here, the bimolecular association rate plays a role, but other factors are equally important, such as the density of capture proteins and the way in which they are immobilized on the particle surface. For example, the capture rate will be high in case capture proteins are present at a high density with their binding sites oriented towards the fluid, compared to the case that only few capture proteins are present and have their binding sites oriented in-plane with respect to the particle surface. These aspects, including the bimolecular association rate constant, are all reflected by the (particle-based) association rate constants determined in our experiments.
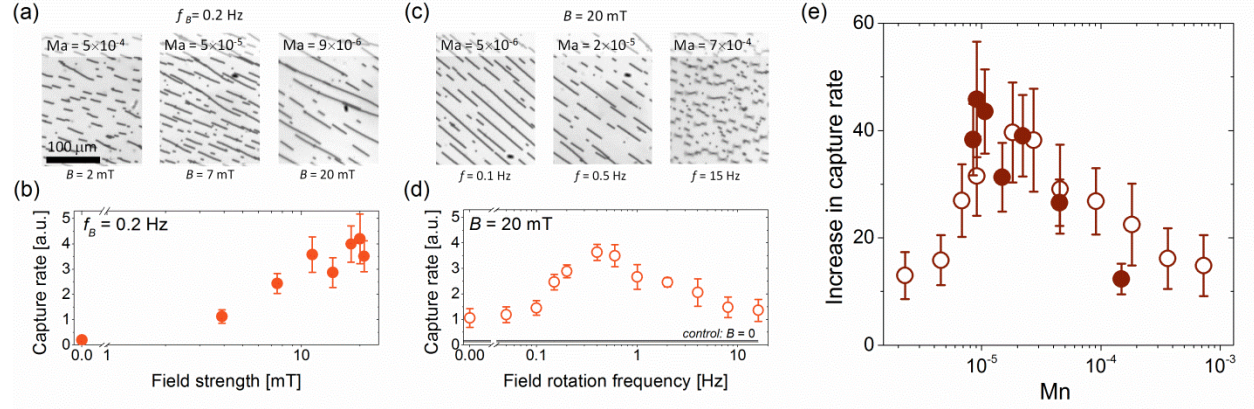
S7 Influence of field rotation parameters

Figure S5. Target capture by magnetically actuated ensembles of magnetic particles for different field rotation frequencies ω and magnetic field strengths B. (a) Microscope images of particle chains for varying B and ω = 0.2 Hz. (b) The corresponding association rate constants. (c) Microscope images of particle chains for varying ω and B = 20 mT. (d) The corresponding association rate constants. (e) Relative increase in k_a compared to no actuation for different Mason numbers, as corresponding to data in panel b and d, respectively represented by the closed circles (●) and the open circles (○). The applied field rotation was alternated in-plane and out-of-plane.

We also investigated the influence of chain rotation on the capture rate. In a rotating magnetic field, magnetic particles form into chains and experience a magnetic torque to align the chains with the (rotating) field. The magnetic torque is opposed by hydrodynamic drag, and depending on the ratio of these interactions the chains can or cannot follow the rotating field. This behavior can be characterized by the dimensionless Mason number[3]:

$$Ma = \frac{\eta\omega}{\mu_0 MH} \equiv \frac{4\pi R_{MP}^3 \eta\omega}{3mB},$$ (S.4)

For high Mason numbers, chains show breaking-and-reformation behavior, inducing chaotic fluid mixing.[3,4] Optimal mixing effects have been reported[3,5] to occur when chains show breaking-and-reformation behavior with relatively long chain fragments. In case rotating chains remain rigid, no chaotic mixing is induced[4]; and when the fragmented chains are short, mixing is only effective close to the original chain.

We have quantified association rate constants for different Mason numbers by varying the magnetic field strength and by varying the rotation frequency of the rotating field. For increasing field strength, see Figure S5a,b, longer chains are formed and the association rate constant is the highest for the maximum field strength that can be generated. While the chain length influences the volume that is mixed, it is not represented within the Mason number.[6] Furthermore, the Mason number is defined for an isolated chain of

particles, whereas in our experiments the chains interact with other chains and become longer if the field strength is increased. As longer chains mix over a larger volume, it is reasonable that k_a is highest for the highest field strength.

For varying rotation frequencies of the magnetic field (see Figure S5c,d), we do observe that an intermediate field rotation frequency is optimal for rapid target capture. For larger frequencies, particle chains remain relatively short (see Figure S5c; similar to low field strengths) and show less mixing[5]. For lower frequencies, long slowly rotating chains are formed (see Figure S5c; similar to high field strengths), which decreases k_a, and in the limit $\omega = 0$ mixing is completely absent. Rotation of the particle chain enhances target capture only when the particle displacement is large compared to the diffusion of the targets. This aspect is not reflected in the Mason number, but in the Péclet number, describing the relative contribution of advective and diffusive transport. For a chain with a length of 15 ± 5 particles, random diffusion over a similar length is achieved in a time period corresponding to a field rotation frequency of 0.06 ± 0.04 Hz. Below this frequency, chain rotation is not effective anymore to enhance the capture rate. Consequently, the optimal field frequency is governed by a balance between on the one hand the rate of mixing and on the other hand the mixed volume. This implies that the frequency should not be too low or too high, but intermediate.

In Figure S5e, the relative increase in k_a with respect to no actuation is plotted for the combined data-sets of varying B and ω, but now expressed in terms of the corresponding Mason numbers (Eq. 7). The different datasets are found to show considerable overlap, indicating that the Mason number is still useful to roughly assess the capture behavior of rotating particle chains, in spite of neglecting the influence of the chain length and diffusion. Figure S5e shows an apparent optimal capture regime at a Mason number of $(1.8 \pm 1.0) \times 10^{-5}$, with an increase in capture rate by a factor 40 ± 10.

S8 Numerical Brownian dynamics simulations of target capture

The particle-based capture process was numerically simulated using Brownian dynamics.

We simulated the dynamics in a rectangular fluid cell with a variable width (e.g., 100 μm) and a height equal to the experimental incubation chamber, namely 600 μm. The fluid cell contains a single spherical magnetic particle with a radius of $R_{MP} = 1.4$ μm that is moved up and down through the fluid cell at different velocities due to an applied field gradient, i.e.

$$v_{MP} = \frac{m}{6\pi\eta R_{MP}} \frac{dB}{dz}.$$
(S.5)

Here, m is the magnetic moment of the particle[7], and η the dynamic viscosity of the fluid. As targets, spherical particles were assumed with a hydrodynamic radius of $R_{IgG} = 5.5$ nm which is equal to the reported hydrodynamic radius of antibodies in PBS[8]. Initially, these particles are randomly distributed over the simulated volume and for each particle we compute the random displacement and rotation due to Brownian motion as well as hydrodynamic interactions due to the movement of the magnetic particle through the fluid. Interactions between the target particles were neglected because target concentrations are dilute.

The random displacement of target particles in all directions, Δr, corresponding to Brownian motion over a discrete timestep Δt follows from the fluctuation-dissipation theorem: (e.g. see Grassia et al.[9])

$$\Delta r_i = n_{rand,3} \sqrt{\frac{24 k_B T}{6\pi\eta R_{IgG}}} \Delta t,$$
(S.6)

in which $n_{rand,3}$ is a 1x3 vector with random numbers, chosen independently at each numerical time-step from a normalized Gaussian distribution with zero mean and variance 12^{-1}. Similarly, we also compute the orientation, i.e., $\theta \in [0, \pi]$ and $\varphi [-\pi,\pi)$, of each target, which is subjected to Brownian rotation about three axes (x, y and z):

$$\Delta \alpha = n_{rand,3} \sqrt{\frac{24 k_B T}{8\pi\eta R_{IgG}^3}} \Delta t.$$
(S.7)

Hydrodynamic interactions acting on targets due to the moving magnetic particle are accounted by computing the flow field u due to a sphere moving through a fluid, i.e.[10]

$$u = \frac{1}{8\pi\eta\Delta r}\left[\left(F + \frac{(\Delta r \cdot F)\Delta r}{\Delta r^2}\right) + \frac{R_{MP}^2}{\Delta r^2}\left(\frac{1}{3}F + \frac{(\Delta r \cdot F)\Delta r}{\Delta r^2}\right)\right].$$
(S.8)

Here, Δr is the center-to-center distance between the target and the magnetic particle, and F is the force acting on the magnetic particle, which is the magnetic gradient force. Based on the small size of the target particles we assume that the target particles are dragged along with the induced flow.

In the simulations, the following boundary conditions were applied to a rectangular unit cell with a height of 600 μm, and width and length of 100 μm. To the top and the bottom of the cell, reflective boundary conditions were applied representing the boundaries of the incubation chamber. To the sides, periodic

boundary conditions were applied. Considering that one magnetic particle is initially situated in the bottom center of the unit cell, the periodic boundary conditions imply a periodicity of particles over the surface. Basically, the particles are ordered in a square lattice with a unit cell with a width of 100 μm. As a result, varying the width of the unit cell alters the initial concentration of particles at the surface. Lastly, the boundary of the magnetic particle is treated as being partially absorbing, i.e. binding only occurs for angular differences smaller than a pre-defined angle $\alpha \in [0, \pi]$ between (i) the orientation vector of the target and (ii) the relative position vector between the particle and the target. In other words, the target needs to orient itself towards the magnetic particle to bind. In case $\alpha = \pi$, targets "bind" to the particle independent of their orientation. In case of $0 < \alpha < \pi$, targets only bind for a limited range of orientations, and otherwise reflect from the surface. In this way, constraints to the relative orientation can be imposed. Lastly, the time-steps were chosen to be 3 μs, which is small enough to keep propagation errors negligible (see Figure S6) which is important for a reliable outcome of a forward Euler method. So, for time-steps of 3 μs, the outcome of the numerical simulations is independent of the time-step.
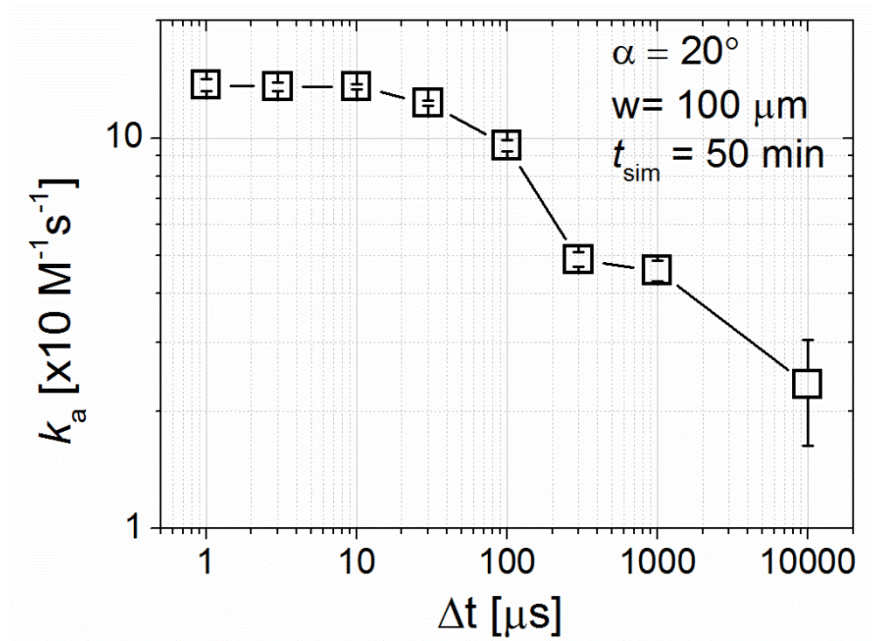

Figure S6 Influence of the numerical time-step on the association rate constant as obtained from least-squares linear fits to simulated binding data. For time-steps below 10 μs, the found association rate constant does not depend on the time-step anymore.
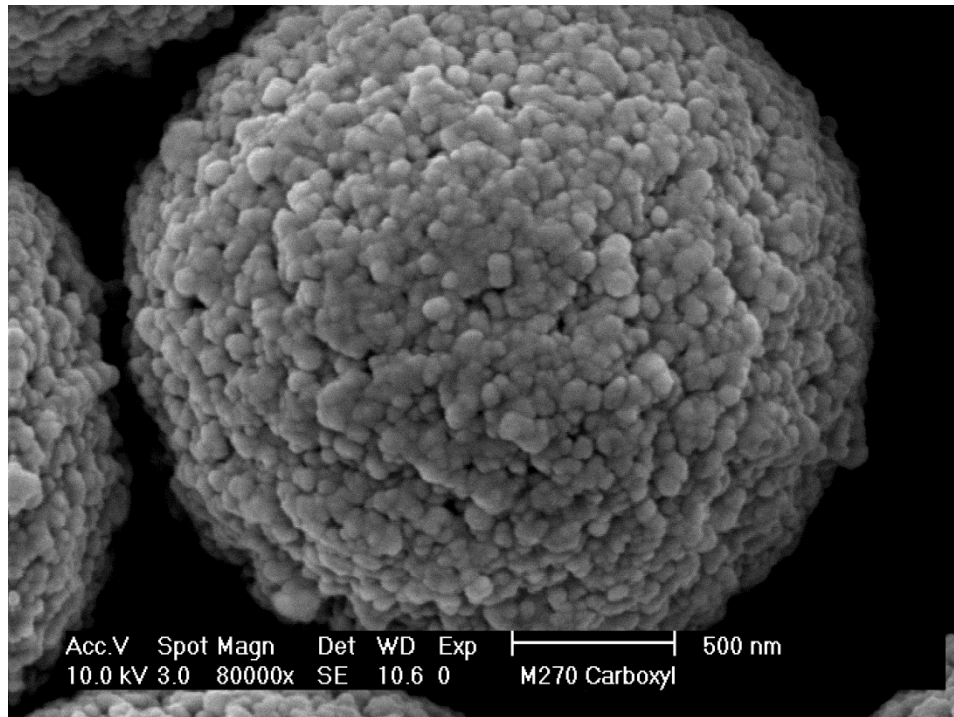
S9 SEM picture of M270 magnetic particles

Figure S7 Scanning Electron Microscope image of a Dynal M-270 superparamagnetic particle before protein G is covalently coupled to the carboxyl groups by EDC-NHS coupling chemistry. From these images we estimate that surface irregularities have dimensions which are in the range of 10-200 nm.

References

(1)   Van Reenen, A.; de Jong, A. M.; Prins, M. W. J. *Lab Chip* **2015**, 15, 2864

(2)   Homola, J.; Yee, S. S.; Gauglitz, G. *Sensors and Actuators B-Chemical* **1999**, *54*, 3–15.

(3)   Kang, T.; Hulsen, M.; Anderson, P.; den Toonder, J.; Meijer, H. *Phys. Rev. E* **2007**, *76*, 066303.

(4)   Gao, Y.; van Reenen, A.; Hulsen, M. A.; de Jong, A. M.; Prins, M. W. J.; den Toonder, J. M. J. *Microfluid. Nanofluidics* **2013**, *14*.

(5)   Lee, J. T.; Sudheendra, L.; Kennedy, I. M. *Anal. Chem.* **2012**, *84*, 8317–8322.

(6)   Gao, Y.; Hulsen, M. A.; Kang, T. G.; den Toonder, J. M. J. *Phys. Rev. E* **2012**, *86*, 41503.

(7)   Van Reenen, A.; Gao, Y.; Bos, A. H.; de Jong, A. M.; Hulsen, M. A.; den Toonder, J. M. J.; Prins, M. W. J. *Appl. Phys. Lett.* **2013**, *103*, 043704.

(8)   Weiss, M.; Elsner, M.; Kartberg, F.; Nilsson, T. *Biophys. J.* **2004**, *87*, 3518–3524.

(9)   Grassia, P. S.; Hinch, E. J.; Nitsche, L. C. *J. Fluid Mech.* **1995**, *282*, 373–403.

(10)   Kundu, P. K.; Cohen, I. M.; Dowling, D. R. *Fluid Mechanics - 5th Ed.*; Elsevier: Amsterdam, 2012.